The Astrophysical Journal, 993:223 (13pp), 2025 November 10 https://doi.org/10.3847/1538-4357/ae0a21

A Multiwavelength View of the Multimessenger Sources NGC 1068 and PKS 1502+106

Abhishek Desai[1], Stefano Marchesi[2,3,4], Justin Vandenbroucke[5], Indrani Pal[3], Ke Fang[5], Dieter Hartmann[3], Regina Caputo[6], Marco Ajello[3], Jessie Thwaites[5], Kavic R Kumar[6,7], and Sam Hori[5]
[1] NASA Postdoctoral Program Fellow, NASA Goddard Space Flight Center, Greenbelt, MD 20771, USA; adesai.physics@gmail.com
[2] Dipartimento di Fisica e Astronomia (DIFA), Università di Bologna, via Gobetti 93/2, I-40129 Bologna, Italy
[3] Department of Physics and Astronomy, Clemson University, Kinard Lab of Physics, Clemson, SC 29634-0978, USA
[4] INAF—Osservatorio di Astrofisica e Scienza dello Spazio di Bologna, Via Piero Gobetti 93/3, 40129 Bologna, Italy
[5] Dept. of Physics and Wisconsin IceCube Particle Astrophysics Center, University of Wisconsin–Madison, Madison, WI 53706, USA
[6] NASA Goddard Space Flight Center, Maryland, USA
[7] University of Maryland, College Park, Maryland, USA
Received 2025 August 13; revised 2025 September 19; accepted 2025 September 20; published 2025 November 6

Abstract

Multimessenger astronomy offers a powerful approach to studying high-energy radiative processes in astrophysical sources. A notable example was seen in 2017, when the IceCube Neutrino Observatory detected a high-energy neutrino event that was found to coincide with a gamma-ray flare from a blazar. Since then, numerous multimessenger studies combining neutrino and photon data have been conducted, yet the origin of neutrinos from active galactic nuclei (AGN) remains uncertain. In this work, we present the results of an X-ray observing program targeting two AGNs, NGC 1068 and PKS 1502+106. The multiwavelength dataset includes new observations from NICER and NuSTAR from the observing proposal, along with gamma-ray data collected using Fermi-LAT, and one archival observation from Chandra. Additionally, we derive the neutrino fluxes for both AGNs using 10 yr of IceCube data and neutrino spectra predicted by theoretical models. These results demonstrate the importance of combining multimessenger data in building and constraining theoretical models. They also highlight the importance of testing model predictions against observational data to refine measurements of both the neutrino flux and spectral shape.

Unified Astronomy Thesaurus concepts: Active galactic nuclei (16); High energy astrophysics (739); Blazars (164); Seyfert galaxies (1447); Neutrino astronomy (1100); X-ray astronomy (1810); Gamma-ray astronomy (628)

1. Introduction

Active galactic nuclei (AGN) are among the most promising candidates for explaining the extragalactic neutrinos observed by the IceCube Neutrino Observatory at the South Pole. However, the exact nature of the processes that lead to the creation of these neutrinos remains unclear. The first AGN identified as a neutrino source candidate, TXS 0506+056, is a flaring blazar. It was discovered through a multiwavelength campaign (IceCube Collaboration et al. 2018) and supported by a retrospective identification of a neutrino burst from the same source in 2014–2015 (IceCube Collaboration et al. 2018). Using 10 yr of IceCube data, time-integrated searches identified a Seyfert II galaxy, NGC 1068, as a potential neutrino source at a significance of 4.2σ (IceCube Collaboration et al. 2022). IceCube Collaboration et al. (2020) report three additional neutrino source candidate blazars, namely TXS 0506+056, PKS 1424+240, and GB6 J1542+6129. More recently, IceCube Collaboration et al. (2025) found two more non-jetted AGN, namely NGC 4151 and CGCG 420-015, which displayed an excess of neutrinos (2.7σ and 2.8σ, respectively) with respect to background signals. A separate analysis (IceCube Collaboration et al. 2025) also found an excess of neutrinos in the direction of NGC 4151 at a significance of 2.9σ.

The sources that have been associated with neutrino detections belong to different AGN classes. Blazars are considerably more luminous in the gamma-ray regime compared to Seyfert AGN due to different viewing angles with respect to the observer. Several theoretical models have been developed to understand the neutrino production in AGNs (see, e.g., X. Rodrigues et al. 2021; K. Fang et al. 2023; K. Murase & F. W. Stecker 2023).

In jetted AGN models, high-energy neutrinos are produced by the photomeson production process between relativistic protons accelerated by the jet and target photons inside the jet or external radiation fields. The same protons may also produce gamma-ray emission through proton-induced electromagnetic cascades and proton synchrotron radiation. Such models predict a correlation of neutrino flux with the X-ray as well as gamma-ray photons. Such models were invoked to explain the observations of TXS 0506+056 (see, e.g., H. Zhang et al. 2019) as well as PKS 1502+106 (X. Rodrigues et al. 2021, 2024). The blazar PKS 1502+106 was found to be flaring in the radio regime during the time of a neutrino event originating from the same direction (I. Taboada & R. Stein 2019). Theoretical models (X. Rodrigues et al. 2021, 2024) suggest that the shape of the spectral energy distribution (SED) of the blazar changes when the blazar goes from quiescent to flaring state. This change has been observed across the multiwavelength photon regime while also affecting the neutrino emission.

The neutrino production theory is different for non-jetted AGNs, which are generally classified as unobscured or obscured depending on their measured hydrogen line-of-sight column density being below or above the $10^{22}\,\mathrm{cm}^{-2}$ threshold,

respectively. For these AGN, high-energy neutrinos may be produced in various regions of the source, such as the AGN cores and starburst regions. Given that the observed neutrino flux from NGC 1068 and other Seyfert galaxies significantly exceeds the gamma-ray flux, models inspired by IceCube observations have focused on the coronal region as the site of neutrino production. In these models, protons are accelerated by stochastic processes in turbulent magnetic fields (K. Murase et al. 2020) or by magnetic reconnection (D. F. G. Fiorillo et al. 2024). They interact with X-ray photons from coronal electrons and with nearby thermal protons, producing charged pions that decay into neutrinos. Proton interactions with X-ray photons also generate gamma rays from synchrotron or Inverse Compton processes of electron–positron pairs generated via the Bethe–Heitler process, which then cascade down to MeV energies (Y. Inoue et al. 2020; K. Murase et al. 2020). Such coronal models indicate a correlation between the neutrino and X-ray fluxes (A. Khatee Zathul et al. 2025).

For both of the above cases, a possible correlation between X-rays and neutrinos exists. We aim to study this correlation using a NICER monitoring campaign and a systematic analysis of the X-ray observations of two individual AGN sources (one blazar and one Seyfert galaxy), along with the data collected by IceCube. We also add gamma-ray observations from Fermi-LAT to test the gamma-ray connection. For the purpose of this study, we require both AGNs to be possible or confirmed neutrino sources with relevant archival theoretical models explaining the multimessenger emission.

The blazar source used for this study, PKS 1502+106, is reported as a possible neutrino source by I. Taboada & R. Stein (2019) and modeled by X. Rodrigues et al. (2021, 2024). Due to PKS 1502+106 being a known variable source (see, e.g., A. A. Abdo et al. 2010) and due to the detailed theoretical flaring versus quiescent models available in the literature (X. Rodrigues et al. 2021), we choose PKS 1502+106 over other neutrino sources like TXS 0506+056 as the blazar source for the NICER monitoring campaign and this study.

Among the Seyfert galaxies, we choose NGC 1068, which is reported to be the most significant extragalactic neutrino source seen using IceCube IceCube Collaboration et al. (2022). Due to this, neutrino observations of NGC 1068, in addition to photon data, can be used to constrain theoretical models like B. Eichmann et al. (2022), K. Murase (2022). We also chose NGC 1068 as one of the sources for the NICER monitoring campaign to study the short-term fluctuations in the X-ray data of the source.

2. X-Ray Observations

We report in this section the properties of the monitoring campaign of PKS 1502+106 and NGC 1068 using the NICER telescope (K. C. Gendreau et al. 2012) for the Guest Observing Cycle 5 run (proposal ID: 6196, PI: Vandenbroucke). We also discuss the joint NuSTAR observations that were taken as part of this campaign, as well as additional archival observations of the two sources that were taken with other X-ray facilities during the time of the NICER monitoring.

Our monitoring campaigns led to a total of 30 NICER observations (for PKS 1502+106 and NGC 1068) and three joint NuSTAR observations (for PKS 1502+106). Additionally, archival data taken by Chandra on 2024 January 4 (MJD:60313.73) were also used, as it coincided with our NICER observations. More details of the X-ray data used and the analysis performed are given below.

2.1. NICER Observations

Out of a total of 30 NICER observations, we obtained 21 observations for PKS 1502+106 with an observing time of ∼7 ks (spread over 3–4 days), and nine observations for NGC 1068 with an observing time of ∼1 ks for each observation. Two observations of PKS 1502+106 and one observation of NGC 1068 had zero exposure, so they were not included in our analysis. The other 27 nonzero exposure observations were reduced using the steps listed in Appendix A. For each NICER observation, the source signal was compared with the background signal estimated using the `3c50` model given by R. A. Remillard et al. (2022). Using this comparison, the energy range for which the source signal was dominating and the S/N ratio was the highest was selected.

To check the fluctuations of the observed flux over the monitoring period, an initial fit is performed on the NICER observations using the `pgstat` statistical method along with a spectral model. Starting with PKS 1502+106, we use a simple power-law model with Galactic absorption to fit the observed flux. This model is chosen following previous analyses of the same source (see, e.g., A. A. Abdo et al. 2010), where only modest intrinsic X-ray absorption is seen. To model the Galactic absorption, the photoelectric absorption component (TBabs) model is used with a fixed value of $N_{\rm H} = 2.03 \times 10^{20}\,{\rm cm}^{-2}$ (derived using HI4PI Collaboration et al. 2016). The model used to fit NICER observations of PKS 1502+106 is thus given by:

$$TBabs * powerlaw. \quad (1)$$

In the case of NGC 1068, the Galactic absorption model is modified to use a $N_{\rm H} = 3.32 \times 10^{20}$ cm^{-2}, derived using HI4PI Collaboration et al. (2016); this value is fully consistent with the one derived by R. Willingale et al. (2013). As shown by previous analyses of NGC 1068, the intrinsic flux of NGC 1068 cannot be derived using a simple power-law model (see, e.g., M. Guainazzi et al. 1999; S. Bianchi et al. 2001; I. Pal et al. 2022). Additionally, due to a lower signal-to-noise ratio (S/N) found in our NICER observations over a broad energy range, joint observations from another telescope are required to fit a more detailed model (see Section 2.3). As a preliminary check to study the fluctuations in the NICER-only observations, a power-law model is used. In addition, four Gaussian lines are also added to the model to account for any features that can be seen due to emission lines, which occur due to either the source or the NICER instrument. The addition of these Gaussian lines allows for a better fit of the observed spectra after correcting for Galactic absorption. The model used to fit NICER observations of NGC 1068 is thus given by:

$$TBabs * (powerlaw + zgauss + zgauss + zgauss + zgauss). \quad (2)$$

The results of the fit for both the sources, NGC 1068 and PKS 1502+106, are described in Tables 1 and 2, respectively. For each observation, the energy range used for the individual fits is also reported in the Tables.

These initial fits to the NICER observations are used to study the behavior of the two sources over the observing period. This is done by making a light curve and plotting the flux (E^2dN/dE) in units of erg cm^{-2} s^{-1}. As the energy range cannot be different for individual light curve measurements,

Table 1
Best-fit Results for Each NICER Observation of NGC 1068

T_{start} (MJD)	E_{range} (keV)	Normalization (ph keV^{-1} cm^{-2} s^{-1})	Γ_X …	χ^2/DOF …
60005.38	0.3–2.0	$1.47^{+0.09}_{-0.09} \times 10^{-3}$	$4.37^{+0.08}_{-0.07}$	19.6/25
60153.28	0.25–2.0	$3.10^{+0.02}_{-0.02} \times 10^{-3}$	$3.34^{+0.06}_{-0.06}$	25.7/27
60183.04	0.25–2.0	$3.25^{+0.08}_{-0.08} \times 10^{-3}$	$3.31^{+0.03}_{-0.03}$	60.1/30
60215.24	0.25–2.0	$2.66^{+0.09}_{-0.09} \times 10^{-3}$	$3.38^{+0.04}_{-0.04}$	77.8/30
60253.60	0.25–2.5	$2.44^{+0.01}_{-0.01} \times 10^{-3}$	$3.53^{+0.06}_{-0.06}$	81.6/38
60283.23	0.25–2.5	$3.47^{+0.09}_{-0.09} \times 10^{-3}$	$3.24^{+0.03}_{-0.03}$	69.8/37
60314.13	0.25–2.0	$3.28^{+0.01}_{-0.01} \times 10^{-3}$	$3.28^{+0.04}_{-0.04}$	43.1/30
60343.04	0.25–2.5	$3.09^{+0.08}_{-0.08} \times 10^{-3}$	$3.35^{+0.03}_{-0.03}$	74.7/37

Note. The energy bin describes the energy range for which the source signal dominates the background. The observations with zero exposure are not included. The normalization is given in units of photons keV cm^2 s at 1 keV. The Gaussian lines used in the model fit fall around 1.8–2.0 keV, 0.8–0.9 keV, 0.5–0.6 keV, and 1.2–1.3 keV for all the observations.

Table 2
Best-fit Results for Each NICER Observation of PKS 1502+106

T_{start} (MJD)	E_{range} (keV)	Normalization (ph keV^{-1} cm^{-2} s^{-1})	Γ_X …	χ^2/DOF …
NICER Data				
60005.47	0.25–2.0	$3.52^{+0.10}_{-0.10} \times 10^{-4}$	$1.99^{+0.04}_{-0.04}$	97.0/30
60008.32	0.25–2.0	$3.63^{+0.03}_{-0.03} \times 10^{-4}$	$1.87^{+0.15}_{-0.15}$	25.8/26
60031.03	0.25–2.5	$2.68^{+0.07}_{-0.07} \times 10^{-4}$	$2.20^{+0.04}_{-0.04}$	108.9/40
60032.65	0.25–2.0	$2.99^{+0.04}_{-0.04} \times 10^{-4}$	$2.30^{+0.20}_{-0.19}$	26.2/21
60062.86	0.25–3.0	$4.01^{+0.03}_{-0.03} \times 10^{-4}$	$1.68^{+0.14}_{-0.14}$	57.9/36
60063.06	0.25–4.0	$4.90^{+0.01}_{-0.01} \times 10^{-4}$	$1.30^{+0.05}_{-0.05}$	267.1/55
60064.02	0.25–2.0	$3.55^{+0.04}_{-0.04} \times 10^{-4}$	$1.57^{+0.19}_{-0.20}$	19.0/23
60093.06	0.3–2.0	$3.39^{+0.02}_{-0.02} \times 10^{-4}$	$2.96^{+0.09}_{-0.09}$	175.7/25
60123.77	0.3–2.0	$3.20^{+0.01}_{-0.01} \times 10^{-4}$	$1.99^{+0.06}_{-0.06}$	50.3/27
60124.04	0.25–2.0	$2.95^{+0.03}_{-0.03} \times 10^{-4}$	$2.02^{+0.15}_{-0.15}$	49.9/23
60125.14	0.25–2.1	$3.65^{+0.03}_{-0.03} \times 10^{-4}$	$1.82^{+0.14}_{-0.14}$	28.6/25
60158.38	0.25–2.1	$4.84^{+0.02}_{-0.02} \times 10^{-4}$	$1.51^{+0.08}_{-0.08}$	33.9/28
60159.15	0.25–2.0	$3.12^{+0.02}_{-0.02} \times 10^{-4}$	$1.97^{+0.08}_{-0.08}$	53.4/26
60170.06	0.25–2.0	$3.18^{+0.01}_{-0.01} \times 10^{-4}$	$1.92^{+0.06}_{-0.06}$	57.6/29
60171.09	0.25–2.0	$2.54^{+0.04}_{-0.03} \times 10^{-4}$	$2.19^{+0.22}_{-0.22}$	21.6/21
60313.44	0.25–2.0	$2.82^{+0.02}_{-0.02} \times 10^{-4}$	$2.22^{+0.09}_{-0.09}$	53.8/27
60314.02	0.25–2.0	$2.69^{+0.02}_{-0.02} \times 10^{-4}$	$2.33^{+0.11}_{-0.11}$	46.0/26
60315.50	0.25–2.0	$2.94^{+0.01}_{-0.01} \times 10^{-4}$	$2.20^{+0.06}_{-0.06}$	62.5/29
60316.02	0.25–2.1	$3.14^{+0.03}_{-0.03} \times 10^{-4}$	$2.25^{+0.13}_{-0.12}$	38.2/26
NuSTAR Data				
60005.53	5.5–20.0	$1.65^{+0.03}_{-0.01} \times 10^{-4}$	$1.53^{+0.52}_{-0.48}$	36.4/25
60170.01	5.0–15.0	$1.28^{+0.02}_{-0.08} \times 10^{-4}$	$1.51^{+0.45}_{-0.45}$	22.4/21
60343.21	5.0–15.0	$3.04^{+0.04}_{-0.02} \times 10^{-4}$	$1.92^{+0.42}_{-0.41}$	18.9/26

Note. The energy bin describes the energy range for which the source signal dominates the background. The observations with zero exposure are not included. The normalization is given in units of photons keV cm^2 s at 1 keV.

we used a set energy range of 0.3–2 keV for all the observations. We then start with fitting all the NICER observations for a particular source with a power law, while keeping the photon index tied and allowing the normalization to vary in each observation. The derived flux per observation from this joint fit is shown in Section 3 along with Fermi-LAT observations. The derived combined best-fit spectral index (χ^2/DOF) is $\Gamma_X = 2.07 \pm 0.02$(1487.7/491) for PKS 1502+106, and $\Gamma_X = 3.39 \pm 0.02$ (980.5/233) for NGC 1068. The resultant χ^2/DOF is higher for both sources using only NICER data, which can be attributed to the fact that the activity levels of the observations are different, with slightly different spectral shapes. To address this, we add joint observations with NuSTAR (PKS 1502+106) and Chandra (NGC 1068) to the corresponding NICER observation, which improves the fits. The joint fitting for PKS 1502+106 makes use of a power-law model similar to the NICER data fit to derive the intrinsic flux (see Section 2.2). The joint fitting for NGC 1068 used to derive the intrinsic flux makes use of a more detailed model to account for the known spectral complexity of this target (see Section 2.3).

2.2. Joint NICER+NuSTAR Fitting (for PKS 1502+106)

PKS 1502+106 has been observed 3 times with NuSTAR as part of our monitoring campaign: the observations, each ∼20 ks long, were taken in 2023 March (MJD:60005), 2023 August (MJD:60170), and 2024 February (MJD:60343). The steps used to reduce the NuSTAR observations are detailed in Appendix A. The reduced spectra derived from Focal Plane Module A (FPMA) are grouped using the `grppha` tool from Xspec to ensure that there exists a minimum of 70 counts per bin, chosen to reduce the uncertainty per bin from the NuSTAR data. Similar to the NICER fitting, the binned spectra are then fitted using a power law with a Galactic absorption model (*TBabs* ∗ *powerlaw*). The results of the fits are highlighted in Table 2 (bottom three rows).

We also derived the combined best-fit spectral index for the NuSTAR observations (binned between 5 and 15 keV) to be $\Gamma_X = 1.58 \pm 0.32$ (32.55/36). This combined NuSTAR best-fit spectral index for PKS 1502+106 differs from the combined estimate from NICER of 2.08 ± 0.01. This can be attributed to the different energy ranges covered by the satellites, with no overlap after cutting out the spectral regions affected by background (see Table 2). In addition to these individual fits, a joint fit for the observations made with NICER in parallel to NuSTAR was also conducted. Unfortunately, one of the three joint observations of PKS 1502+106, corresponding to the NuSTAR observation made on MJD:60343, had a zero exposure measurement from NICER; so no joint fitting was done. For the other two joint observations, fitting was performed using a power-law model with TBabs, along with a constant scaling factor. The fit model is adapted based on the analysis done by A. A. Abdo et al. (2010) using Swift-XRT and XMM data. The model used is described as:

$$constant * TBabs * powerlaw. \quad (3)$$

All the model parameters are tied together for the NICER and NuSTAR data, while the constant scaling parameter is fixed at 1 for NICER and free to vary for NuSTAR (FPMA observation). This scaling parameter is included to make sure the same model is used for both NICER and NuSTAR data, with an option to vary the normalization for NuSTAR to account for potential cross-instrument calibration offsets. The following results were derived for the two joint fits: for data collected during MJD:60005, the best-fit spectral index is 1.94 ± 0.04 with a χ^2/DOF of 116.1/43. For data collected during MJD:60170, the best-fit spectral index is 1.92 ± 0.06 with a χ^2/DOF of 65.8/39. The results of the joint fits are also

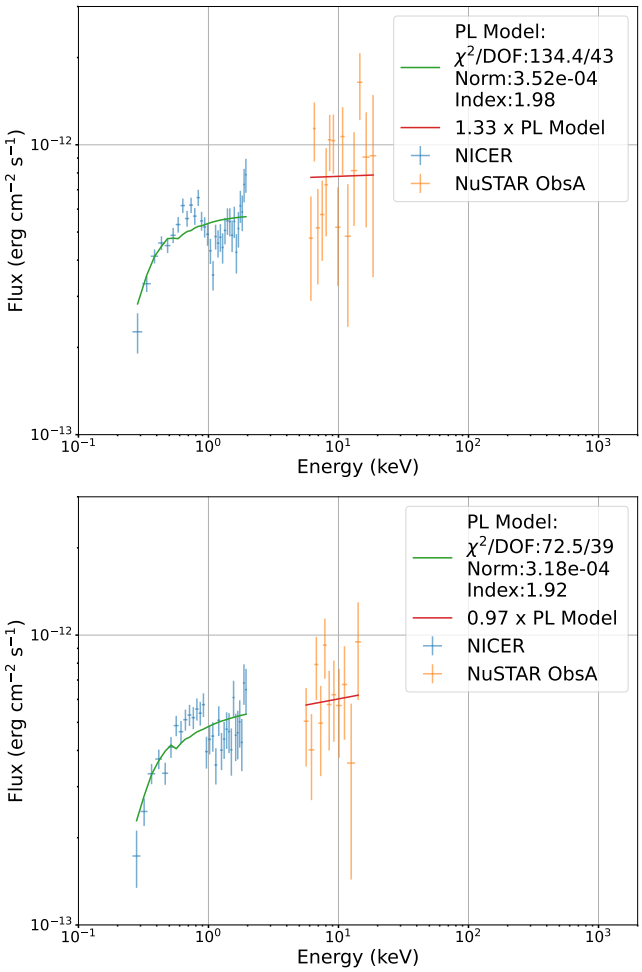

Figure 1. Joint fits for the NICER +NuSTAR observations of PKS 1502+106 made on MJD:60005 (top plot) and MJD:60170 (bottom plot).

shown in Figure 1. The fitting results seen in this study have a much higher χ^2 value as compared to A. A. Abdo et al. (2010). A reason for this discrepancy can be an additional feature seen in the NICER data for this source below 1 keV, which was not seen by the Swift-XRT data used by A. A. Abdo et al. (2010).

2.3. Joint NICER +Chandra Fitting (for NGC 1068)

We searched the X-ray archives for any available X-ray observation of PKS 1502+106 and NGC 1068 taken between 2023 March and 2024 March, which is during the NICER monitoring campaign. We found a Chandra observation of NGC 1068 with Observation (Obs) ID 29071, taken on 2024 January 4 (MJD:60313.73) with an exposure of 10.2 ks (F. Marin et al. 2024), coincident with one of our NICER observations. This Chandra observation is added to the sample and processed jointly with the coincident NICER observation with ObsID 6696021102 and exposure of 10 ks. The steps used to reduce the Chandra observations are detailed in Appendix A.

Once the Chandra observations are reduced, we perform a joint NICER-Chandra fit. K. Iwasawa et al. (1997) and M. Guainazzi et al. (1999) have highlighted the spectral complexity of NGC 1068, far exceeding that of typical Seyfert II galaxies (see also A. B. Romeo & K. Fathi 2016; B. Eichmann et al. 2022). Its continuum includes at least

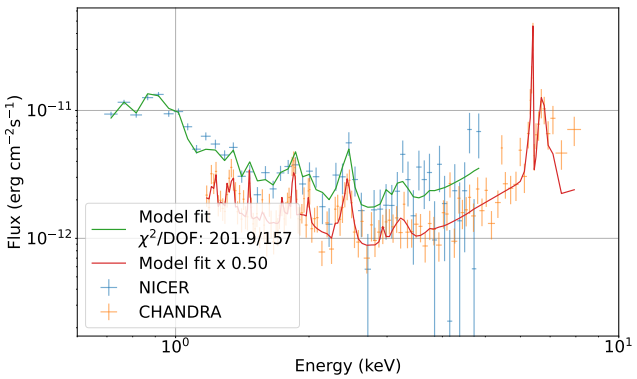

Figure 2. Joint-fit for the NICER +Chandra observation of NGC 1068 is shown here. The NICER observation is made on MJD:60314, and the Chandra observation was conducted on MJD:60313.

three components: a thermal-like emission likely linked to starburst activity detected by ROSAT (A. S. Wilson et al. 1992), a cold reflection component, and a highly ionized reflection component (K. Iwasawa et al. 1997; G. Matt et al. 1997). Numerous emission lines, mainly from ionized gas, are superimposed, although the neutral Fe Kα line is also evident. Following the approach of I. Pal et al. (2022), we adopt an ionization parameter of $\log \xi = 0$ for the cold (neutral) reflector, and $\log \xi$ is kept free to vary for the warm (ionized) reflector.

The final model used to derive the intrinsic flux is expressed as:

$$Model = const * phabs * (mekal + xillver_{cold} + xillver_{warm} + zgauss + zgauss + zgauss + zgauss) \quad (4)$$

where details of the individual model components and the fitting procedure, along with the relevant best-fit and emission line parameters, are given in Appendix B. The model fit is shown in Figure 2. The NICER observations are reduced using the `3c50` background, but we also test this joint fit using the `scorpeon`[8] background and find that the χ^2/DOF is comparable using the two background models.

As discussed above, due to NGC 1068 being a heavily obscured AGN, the observed X-ray spectrum is particularly hard to characterize. In particular, its 0.5–10 keV emission is expected to be dominated by the reprocessed photons coming from the interaction between the intrinsic emission photons and the obscuring medium. The line-of-sight column density of the obscuring medium is $N_{\rm H,los} > 10^{25}\,{\rm cm}^{-2}$, which prevents a clear detection of the intrinsic emission (F. E. Bauer et al. 2015; A. Zaino et al. 2020). Nonetheless, the broadband fit we performed allowed us to obtain an estimate of the intrinsic flux of the primary component, which varies in the range $\sim$(3–4) $\times$ 10^{-10} erg cm^{-2} s^{-1} in the 2–10 keV energy range. This is then compared with the results of F. E. Bauer et al. (2015) to derive the 2–10 keV intrinsic flux from this work. We use a simple power law with photon index $\Gamma = 2.1$ and 2–10 keV luminosity $\log(L_{2-10}) = 10^{43.1}$erg s^{-1}, as reported in F. E. Bauer et al. (2015). This power-law measurement is thus used as the intrinsic flux, $F_{\rm int}$ along with the observed data points shown in Figure 2, to compare the neutrino spectrum in Section 4.

[8] https://heasarc.gsfc.nasa.gov/docs/nicer/analysis_threads/scorpeon-overview/

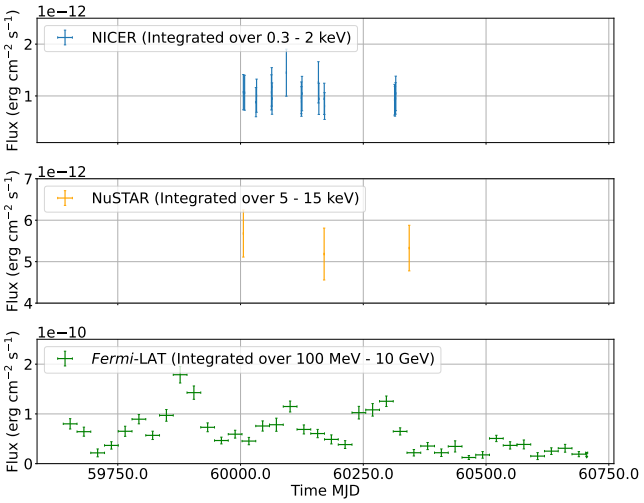

Figure 3. Light Curve for PKS 1502+106 derived using the data collected by NICER (top panel), NuSTAR (middle panel), and Fermi-LAT (bottom panel) is shown here.

3. Gamma-Ray Data Using Fermi-LAT

For both of the sources in our sample, we start by using 3 yr of Fermi-LAT data spanning from 2022 March (MJD:59639) to 2025 March (MJD:60735). The Pass-8 class data contains "SOURCE" photons that are binned over an energy range of 100 MeV to 10 GeV and are used for this study. The dataset is also filtered with a zenith angle of 90°. A region of interest (ROI) of 10° around the source position is used along with the data filters given by "DATA_QUAL>0 && LAT_CONFIG==1" and an angular separation of 15° from the Sun. A sky model is then constructed comprising emission from background sources, diffuse Galactic emission, and diffuse extragalactic emission.[9] The background sources are found using the gamma-ray sources detected in the fourth Fermi-LAT DR3 catalog (S. Abdollahi et al. 2022) and located inside a 15° ROI around the source position, to account for photon leakage. A binned likelihood method was used for the study, along with the "P8R3_SOURCE_V3" LAT instrument response function. Similar to the X-ray study, we first derive the Fermi-LAT light curve for the two sources to check for any major flaring activity. As shown in Figures 3 and 4, no significant flaring activity is seen for both of the sources over the 3 yr period considered in this study.

Two sets of SEDs for the Fermi-LAT data integrated over a period of 1 week and over a period of 3 yr are then created. PKS 1502+106 shows some variation in the gamma-ray flux dataset (see Figure 3). So for each NICER observation made on the time given in Table 2, a ±3.5 days (giving a total of 1 week) Fermi-LAT observations are used to report the final SED. On the other hand, NGC 1068 is a Seyfert galaxy and not bright in gamma rays, and also had no significant variability seen in the generated light curve (Figure 4). The Fermi-LAT data taken over a duration of 3 yr is used to create the SED of NGC 1068. Both of the resultant SEDs are discussed in more detail in Section 4.1 (for PKS 1502+106) and Section 4.2 (for NGC 1068).

[9] The Galactic template gll_iem_v07.fits and the extragalactic template iso_P8R3_SOURCE_V3_v1.txt are used here and taken from https://fermi.gsfc.nasa.gov.

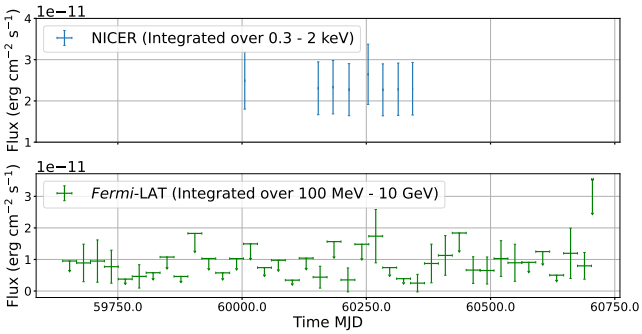

Figure 4. Light Curve for NGC 1068 derived using the data collected by NICER (top panel) and Fermi-LAT (bottom panel) is shown here. The X-ray observations are taken between 2023 March (MJD:60004) to 2024 February (MJD:60341), while the Fermi-LAT light curve is derived using 4 week time bin periods from 2022 March (MJD:59639) to 2025 March (MJD:60735).

4. Comparing to Multimessenger Model Predictions

Before comparing the multimessenger observations to model estimates, the neutrino flux measurements have to be derived. To obtain the neutrino flux measurements and upper limits (in case of a nondetection), we make use of the `SkyLLH` tool described by C. Bellenghi et al. (2023). This work makes use of the 10 yr IceCube neutrino data (IceCube Collaboration et al. 2021b, 2021c) sample, which consists of track-like neutrino events. To test the `SkyLLH` setup, we first use a power-law spectral model as the source neutrino spectrum and compare it to the limits reported by IceCube Collaboration et al. (2020). We use PKS 1502+106 as the test source and derive an upper limit of 6.1×10^{-13}(TeV^{-1} s^{-1} cm^{-2}), which is compatible with the upper limit reported by IceCube Collaboration et al. (2020) of 2.9×10^{-13}(TeV^{-1} s^{-1} cm^{-2}). The discrepancy in the limits is a result of the reduced sensitivity of the public data analysis due to the detector response matrix binning, resulting in a slightly higher upper limit (see also C. Bellenghi et al. 2023, for more details). While theoretical models (X. Rodrigues et al. 2021; B. Eichmann et al. 2022; K. Murase 2022) are used to derive the neutrino flux measurements or upper limits, no joint fitting is performed with the X-ray and gamma-ray observations presented in this work.

4.1. PKS 1502+106

The blazar PKS 1502+106 has only been reported to have neutrino upper limits derived using a power-law source spectrum by IceCube (IceCube Collaboration et al. 2020). Studies like X. Rodrigues et al. (2021) show that the predicted neutrino spectral shape can be different from a power law, making a direct comparison of the existing limits with neutrino theoretical models difficult. To address this, we use `SkyLLH` to change the neutrino source model to match the theoretical model, allowing us to put constraints on a particular model. We use a likelihood setup similar to the one described in C. Bellenghi et al. (2023), along with the Minuit minimizer. Additionally, in our `SkyLLH` setup, the probability density functions (PDFs) used are based on kernel density estimation (KDE). As described by T. Kontrimas & M. Wolf (2021), the KDE method is a nonparametric approach that improves the PDF construction of the point-source analysis, improving the statistical power of the study. Additional details about the

likelihood framework used with SkyLLH are given in Appendix C.

For this work, we test the quiescent and flaring (Hard and Soft Flare) leptohadronic models reported by X. Rodrigues et al. (2021) and use them as the injected source spectrum as opposed to a simple power law. While there exist additional multimessenger models like X. Rodrigues et al. (2024), we choose the X. Rodrigues et al. (2021) model to be tested here, due to the separately modeled quiescent and flaring curves. We change the injected neutrino source spectra in our setup from a simple power law to a log parabola (LP)-like shape. The LP-like spectrum is similar to the estimation by X. Rodrigues et al. (2021) and makes our likelihood dependent on the peak energy and normalization parameters for the neutrino flux distribution curve. Note that the shape of the spectrum is not fitted, and only the peak energy and normalization can be varied in this test. For all three cases, we fix the peak energy of the distribution based on the model being tested. This ensures that in case of a nondetection, the reported upper limits can be used to put constraints on the theoretical model being tested.

No significant neutrino emission is seen when compared to the background for all three cases, so we derive the upper limits and show them as solid lines in Figure 5. While the quiescent and Soft Flare neutrino model predictions of X. Rodrigues et al. (2021) lie below our measured upper limits, the hard-flare model can be ruled out based on the derived neutrino upper limits from our study (see also F. Oikonomou et al. 2021, which reports a similar conclusion).

4.2. NGC 1068

The Seyfert galaxy, NGC 1068, has been detected by IceCube (IceCube Collaboration et al. 2022) with a neutrino flux measurement that makes use of a power law with a best-fit spectral index of 3.2 ± 0.2. There exist theoretical multi-messenger models (B. Eichmann et al. 2022; K. Murase 2022) to explain this measured neutrino flux. These models make use of available multiwavelength photon data along with the neutrino measurements to predict the neutrino flux spectrum. While the models use the IceCube power-law flux measurement to fit their spectrum, the shape of the neutrino spectrum follows an LP-like curve with a peak energy that varies based on the model presented. The neutrino model from B. Eichmann et al. (2022) has a peak energy of ∼35 GeV. This peak energy changes to ∼822 GeV for the model presented by K. Murase (2022), for the *pp* scenario with $\xi_B = 0.01$, where ξ_B is used to parameterize the magnetic field of the AGN. We use our `SkyLLH` setup to change the neutrino source spectrum from a simple power law to an LP-like curve following a spectral shape given by the B. Eichmann et al. (2022) and K. Murase (2022) models. The neutrino spectral shape is kept similar to the model tested, and the only parameters fitted are the peak energy and the normalization, making it a rigid horizontal shift or a scaled vertical shift of the model. This allows us to put updated constraints on the neutrino flux measurement and also allows us to test the model estimates with neutrino data.

We test five different cases for the source model. Case 1 makes use of a simple power-law model, which serves as a comparison of our setup with the results reported by IceCube Collaboration et al. (2022). Cases 2 and 3 substitute the power-law source model with a neutrino spectrum that has a fixed shape similar to the B. Eichmann et al. (2022) neutrino model (dubbed as "Eichmann model" from this point). In Case 2, we fix the peak energy parameter, while in Case 3, the peak energy parameter is allowed to vary. Similarly, Cases 4 and 5 make use of a neutrino model spectrum which follows a shape similar to the K. Murase (2022) model, estimated for the minimal *pp* scenario with $\xi_B = 0.01$, where ξ_B is used to parameterize the magnetic field of the AGN (dubbed as "Murase model" from this point). Similar to the previous case, Case 4 fixes the peak energy parameter to the model estimate while Case 5 allows the peak energy parameter to vary. For each of the cases, the local p-value, denoted as $-\log_{10} p_{\rm local}$, which serves as the detection of the source as compared to the background, is computed. Note that the background is computed based on the spectral information, and the reported test statistic (TS) and $-\log_{10} p_{\rm local}$ do not exhibit a monotonic relationship due to varying degrees of freedom and spectral shapes across cases. Finally, the best-fit parameter values are computed along with uncertainties and the best-fit TS and reported along with $-\log_{10} p_{\rm local}$ in Table 3.

We first compare the results reported by IceCube Collaboration et al. (2022) to the flux we derive using a power-law neutrino source model (denoted as Case 1). We find that our best-fit spectral index matches almost exactly with IceCube Collaboration et al. (2022), while the flux is found to be compatible within uncertainties. The difference in the flux normalization values can be attributed to the difference in the neutrino data samples used for the two studies and the detector response matrix binning for `SkyLLH`. We then move to Case 2–5 to find that the derived $-\log_{10} p_{\rm local}$ does not vary significantly for these tested cases. The best-fit TS changes to account for the additional degree of freedom in the case of Cases 3 and 5. While the fixed peak energy cases (Cases 2 and 4) are useful to provide normalization limits on the tested models, the free peak energy tests help us understand if the tested model is preferred by the neutrino data.

We start with Case 3, which uses the Eichmann model with the peak energy allowed to vary. We derive a flux measurement which is a factor of 10 higher than the model and a best-fit peak energy of 3.4 GeV, which is outside the sensitivity range of the point-source tracks neutrino data sample (∼100 GeV–1 PeV; see IceCube Collaboration et al. 2021c). Due to this, while the best-fit results from Case 3 are reported in Table 3, they are not used to extrapolate a flux at energies less than the peak energy, similar to Case 2. However, we can still use the best-fit results from Table 3 to understand why a lower best-fit energy is preferred by the model. This case has two degrees of freedom, peak energy ($E_{\rm peak}$) in GeV and normalization derived by fitting the number of neutrino signal events (n_s). We use different combinations of $E_{\rm peak}$ and n_s to derive a likelihood contour profile. A $\Delta{\rm TS}(E_{\rm peak}, n_S)$ value is derived for each combination of $E_{\rm peak}$ and n_S using $\Delta{\rm TS} = {\rm TS}_{\rm bestfit} - {\rm TS}(E_{\rm peak}, n_S)$, where the TS values are derived by using the corresponding likelihood ratios found by subtracting the likelihood at the point tested from the null likelihood. The resultant likelihood profile is shown in Figure 6 (top). Additional lines denoting 68%, 90% and 95% quantiles for a χ^2 distribution with 2 degrees of freedom are also added, assuming Wilk's theorem S. S. Wilks (1938). It is seen from the profile that the fit prefers an energy with maximum upper limit uncertainty of $\log_{10}(1.7)$ or ∼50 GeV, which is already lower than the sensitivity range of the PS tracks neutrino data sample. As the model tested has a rigid

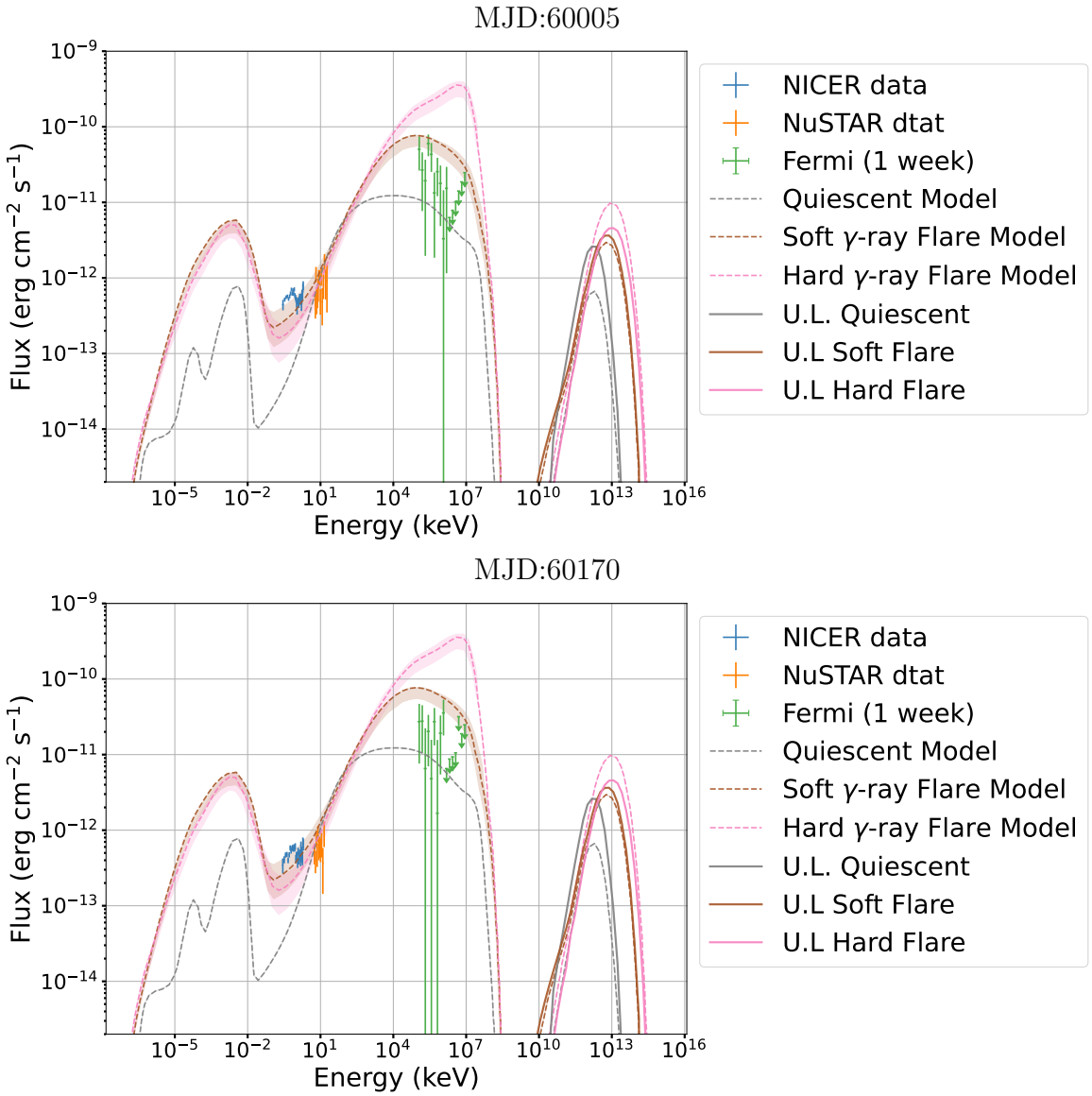

Figure 5. The multiwavelength observations of PKS 1502+106 are shown (top: MJD:60005; and bottom: MJD:60170), with the neutrino limits derived using `SkyLLH` and the theoretical models of X. Rodrigues et al. (2021). No fitting is done in this case, and the models are shown only for comparison. The photon data includes NICER +NuSTAR + 1 week Fermi-LAT observations.

shape, a possible reason for this is that the neutrino observations are trying to fit the higher energy portion of the Eichmann model, shifting the peak energy to lower values. Upon extrapolating the flux using the shape of the Eichmann model, it was seen that the flux measurement and shape of the spectrum closely match to the power-law flux reported by IceCube Collaboration et al. (2022). However, the resultant best-fit flux at the peak energy of 3.4 GeV for this Case will require a proton luminosity that exceeds the bolometric luminosity. This implies that the Eichmann model is not soft enough to fit the neutrino data, and a softer model is required. Note that this setup only shifts the tested model to find the best-fit peak Energy, while the shape of the model is rigid. The `SkyLLH` setup used in this work is not set to fit an additional parameter, which can change the shape of the spectrum. The results of this Case also specify the need for a more detailed fit of the neutrino data with a more generic model to explain this result. Future upgrades to the likelihood fitting, along with future neutrino measurements at lower energies from IceCube detector upgrades (IceCube Collaboration et al. 2021a), will also be able to better understand the flux behavior and update models similar to B. Eichmann et al. (2022).

Similar to Case 3, we test the K. Murase (2022) model in Case 5 by changing the spectral model and freeing the peak energy and n_S. In this case, the best-fit energy lies within the sensitivity range of the PS tracks neutrino data sample $\sim$100 GeV–1 PeV (see IceCube Collaboration et al. 2021c). A likelihood contour similar to Case 3 is also derived for this case and shown in Figure 6 (bottom), which allows us to understand the results reported in Table 3. The Murase model fit also prefers a lower peak energy, with the lower uncertainty limit falling below the peak energy reported by the model (and shown in Case 4). While the detection $-\log_{10} p_{\rm local}$ value for Case 5 is lower than Case 4, the $\rm TS_{fit}$ for Case 5 is higher, with more degrees of freedom and a best-fit peak energy inside the sensitivity range, implying that Case 5 cannot be ruled out.

Table 3
Best-fit Neutrino Results of NGC 1068 Using the Tracks Dataset Observation from IceCube Collaboration et al. (2021b, 2021c)

Case Tested	Index	Peak Energy (GeV)	Neutrino Flux (erg cm^{-2} s^{-1})	$-\log_{10} p_{\rm local}$ (detection)	$\rm TS_{fit}$ (fit)	D.O.F
IceCube Collaboration et al. (2022) (Archival result for comparison)	$3.2^{+0.2}_{-0.2}$	⋯	$8.01^{+2.4}_{-3.01} \times 10^{-11}$	7.0	⋯	2
This work:						
Case 1: Power Law	$3.2^{+0.3}_{-0.3}$	⋯	$5.25^{+1.3}_{-1.3} \times 10^{-11}$	4.33	21.07	2
Case 2: Eichmann Model (Fixed peak energy)	⋯	33.4	$1.01^{+0.27}_{-0.28} \times 10^{-10}$	4.57	19.35	1
Case 3: Eichmann Model (Varying peak energy)	⋯	$3.4^{+48.8}_{-3.3}$	$7.86^{+3.3}_{-2.9} \times 10^{-10}$	4.27	20.73	2
Case 4: Murase Model (Fixed peak energy)	⋯	822.5	$4.01^{+1.2}_{-1.1} \times 10^{-11}$	4.63	18.64	1
Case 5: Murase Model (Varying peak energy)	⋯	$110.2^{+652.4}_{-107.8}$	$1.21^{+4.6}_{-5.1} \times 10^{-10}$	3.96	20.93	2

Note. Three cases are tested based on the neutrino source model used. All the fits for Cases 1–3 are derived using the `SkyLLH` software. The flux measurements shown for the power-law cases of the archival measurement from IceCube Collaboration et al. (2022) and Case 1 (derived in this work) are the best-fit neutrino flux at 1 TeV, while for the rest of the cases, the flux measurement is the best-fit value at the corresponding peak energy. Cases 2–5 shown here make use of the neutrino model prediction reported by B. Eichmann et al. (2022) and K. Murase (2022) as the source model, as opposed to a simple power law. The uncertainties for Case 1 are estimated using the Hessian matrix of the likelihood function. The uncertainties for Case 2–5 are derived using the 1σ contour assuming a χ^2 distribution with the relevant degrees of freedom.

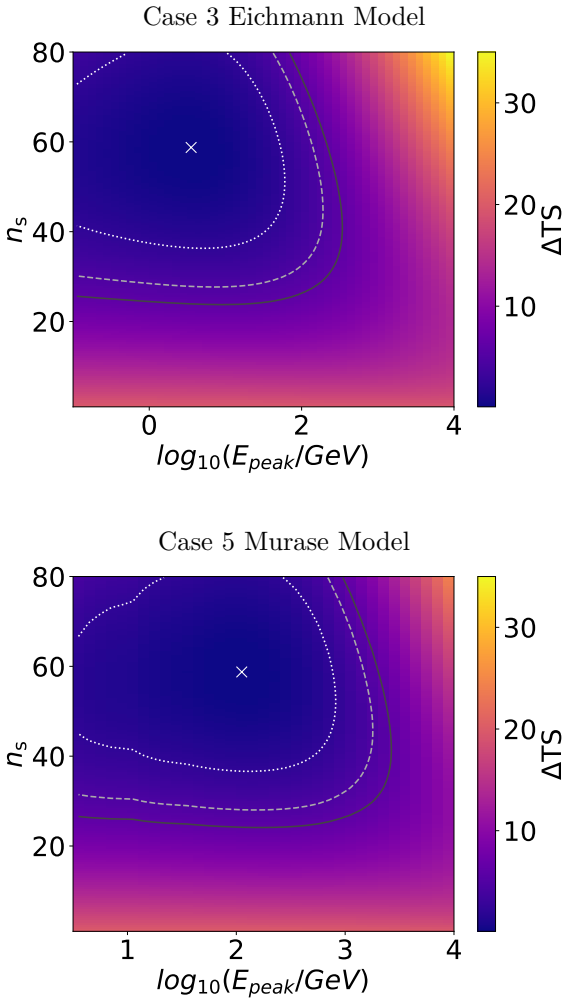

Figure 6. The 2D likelihood profile of $E_{\rm peak}$ and n_S for Case 3 and Case 5 is shown here, where the $\Delta{\rm TS} = {\rm TS}_{\rm bestfit} - {\rm TS}(E_{\rm peak}, n_S)$ is derived for each combination of $E_{\rm peak}$ and n_S. The white (dotted), gray (dashed), and black (solid) lines show the 68%, 90% and 95% contour regions, respectively.

Thus, a flux extrapolation is derived for Case 5, along with Case 4, over a wider energy range and shown in Figure 7 for comparison.

The best-fit measurements for Case 2, Case 4, and Case 5 are used to obtain neutrino flux extrapolation measurements over a wider energy range, which is then reported in Figure 7. This allows us to determine an estimate of the neutrino flux based on the model shape tested at energies $E_\nu < E_{\rm peak}$ and $E_\nu > E_{\rm peak}$. To derive this flux, we first use the shape of the neutrino model from B. Eichmann et al. (2022) and K. Murase (2022), along with the best-fit measurements, and extrapolate over it. This resultant neutrino flux extrapolation is shown in Figure 7 as a black solid line with a gray uncertainty band. While only the models presented in B. Eichmann et al. (2022) and K. Murase (2022) are tested here, the best-fit neutrino measurements change based on the spectral shape of the model tested. This can be seen by comparing the neutrino flux from the tested models in this work and the neutrino flux from IceCube Collaboration et al. (2022). We can see that neutrino models which are harder than the one reported by B. Eichmann et al. (2022) will tend to give a low $E_{\rm peak}$ value ($<$100 GeV), indicating a preference for softer models like that presented in K. Murase (2022). Note that in this work, we do not derive a flux limit over the energy band where IceCube observations are most sensitive (similar to IceCube Collaboration et al. 2022), but derive the flux extrapolation over a wider energy range for better comparison with theoretical models. This is highlighted by the fact that the fluxes derived in this work for NGC 1068 match with the ones reported by IceCube Collaboration et al. (2022) in the region where IceCube observations are most sensitive (highlighted by the red shaded region in Figure 7).

5. Summary and Discussion

In this study we analyzed the photon emission from the blazar PKS 1502+106 and the Seyfert II galaxy NGC 1068, in the X-ray and gamma-ray regimes, along with the neutrino

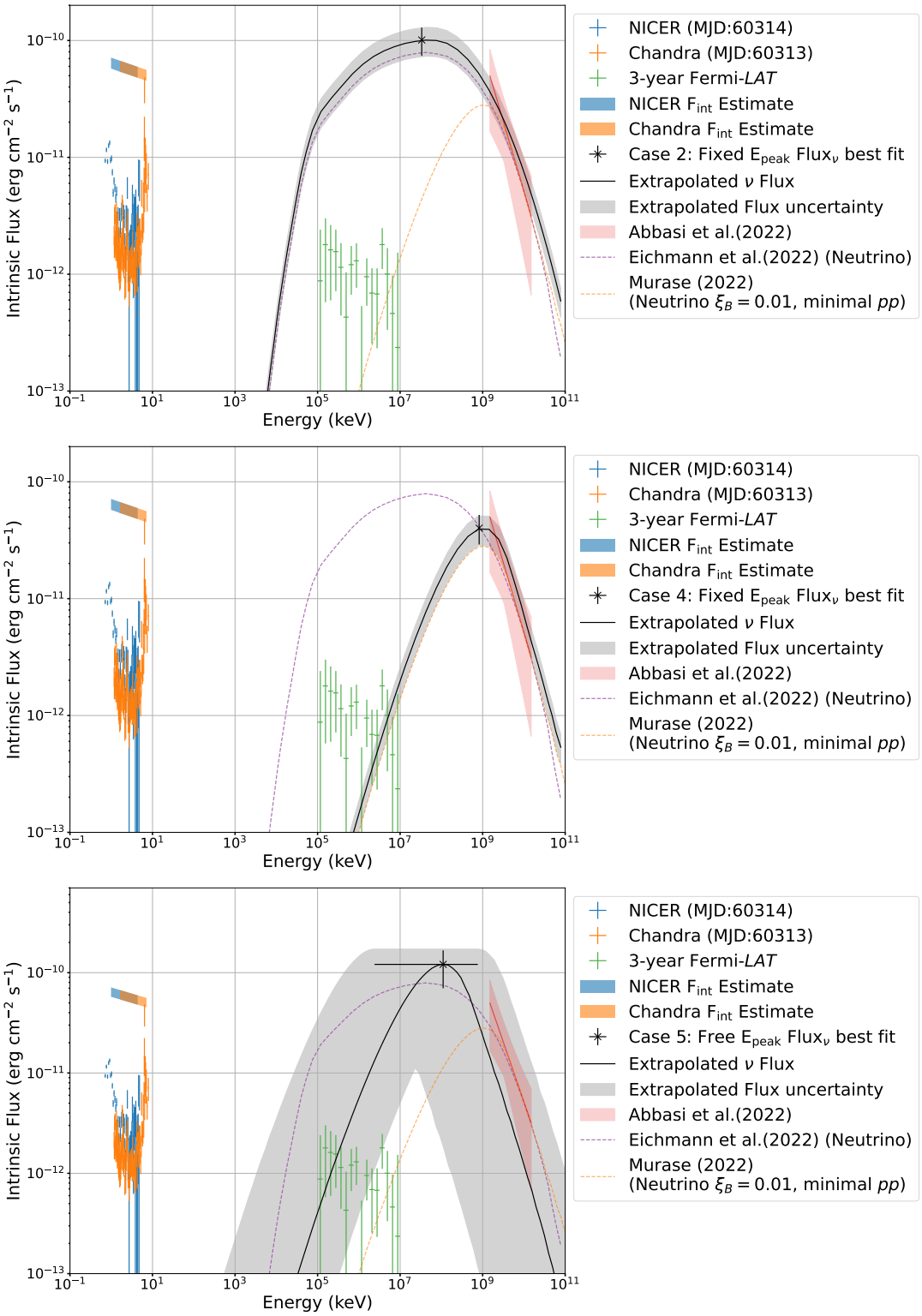

Figure 7. The multiwavelength and multimessenger observations for NGC 1068 are shown with neutrino measurements from IceCube Collaboration et al. (2022; red shaded region). The observations shown here and derived using this study include: (1) The NICER (blue)+Chandra (orange) observed data are shown as data points, while the intrinsic flux $F_{\rm int}$ estimates and the corresponding 90% uncertainties derived from Section 2.3 are shown as the blue and orange shaded regions; (2). The Fermi-LAT observations are shown as green data points (note that the observed Fermi-LAT data are shown here and not the intrinsic measurements); and (3). The neutrino best-fit measurements, for three different neutrino source spectrum cases and derived using `SkyLLH` (see Table 3), are shown as a black data point for each case (Case 2: Top, Case 4: Middle, and Case 5: Bottom Plot). The extrapolated flux over 10 GeV to 10 TeV and the relevant uncertainty are also shown by a black dotted line with a gray shaded region. The theoretical model predictions from B. Eichmann et al. (2022) and K. Murase (2022) are also shown using dashed lines just for comparison.

emission seen by IceCube. We have compared these observed data with theoretical models while fitting the neutrino portion of the model. The results derived for the two sources are different and discussed in more detail below.

5.1. PKS 1502+106

We compare the photon observations and derived neutrino limits for PKS 1502+106 with the model estimates from X. Rodrigues et al. (2021) in Figure 5. Based on only the neutrino upper limits, we see that the modeled neutrino emission is in excess for the hard-flare case, while the modeled emission for the Soft Flare and quiescent cases is consistent with our derived upper limits. While the neutrino upper limits can help rule out the neutrino emission derived using the hard-flare model, the neutrino upper limits alone cannot distinguish between the quiescent and flaring cases. The lightcurves in Figure 3 suggest that while the gamma-ray emission of the source was fluctuating over a $\sim$3 yr period considered here, no significant flaring activity was seen in X-rays during the 1 yr observation period. This implies that the blazar was not flaring during the observation, and the 1 week gamma-ray observation used in Figure 5 coincides with a time when the source was in a quiescent state. Comparing the quiescent model with the Fermi-LAT and NICER data, we find that the model under-predicts the observations. Our results suggest the need to refit the emission model after combining the NICER, NuSTAR, and Fermi-LAT observations along with neutrino upper limits and update the quiescent model.

5.2. NGC 1068

Compared to PKS 1502+106, NGC 1068 is detected by the IceCube data (IceCube Collaboration et al. 2022), enabling a more detailed test of various theoretically motivated spectral models. As summarized in Table 3, we tested LP-like neutrino models using the spectral shape provided by B. Eichmann et al. (2022) or K. Murase (2022), where the peak energy of the spectrum is either fixed to the model estimate (Cases 2, 4) or allowed to vary (Cases 3, 5). In all cases except for Case 3, where the best-fit value of the peak energy falls outside the IceCube sensitivity range (see Section 4.2), the derived flux extrapolations based on the best-fit neutrino flux agree with the measurement of IceCube Collaboration et al. (2022) within uncertainties (see Figure 7). For Cases 2 and 4, where the peak energy is fixed, the model prediction lies below the derived neutrino flux but is still within uncertainties. In Case 5, where the peak energy is freed, the model of K. Murase (2022) yields a large flux at 100 GeV, although the associated uncertainties are large (see also D. F. G. Fiorillo et al. 2024, which reports a similar result). While all existing NGC 1068 neutrino models were not tested in this study, this work highlights the use of IceCube data in similar studies to constrain models based on their best-fit predictions.

The best-fit results derived in this work highlight the need for additional constraints on the neutrino data at lower energies. Such constraints will reduce the uncertainties associated with the best-fit measurements and improve the significance of detections. Future upgrades to the IceCube neutrino detector (IceCube Collaboration et al. 2021a) or the IceCube "deepcore" data would be able to help constrain the models in this lower energy region.

As NGC 1068 is an obscured AGN (see Section 2.3), the derived photon observations from NICER and Chandra for NGC 1068 are difficult to obtain. Based on the observational data collected and the joint photon model tested, intrinsic X-ray flux measurements are derived (in the form of a simple power law), which can then be compared with the neutrino flux measurements. While the model estimates of B. Eichmann et al. (2022) predict only the proton emission, our NICER +Chandra observations are consistent with the background corona estimates shown as the uncertainty band in Figure 5 of B. Eichmann et al. (2022). For this source, while photon measurements alone in the X-ray regime are not able to constrain the model, the neutrino data can help test the validity of the model (see also C. Yuan et al. 2025). While the X-ray models are subject to large uncertainties, the observed gamma-ray flux from Fermi-LAT, shown in Figure 7, can be modeled reasonably well by models like the one presented in B. Eichmann et al. (2022). Future observations in the MeV regime by detectors like AMEGO can also help provide valuable model constraints for this source (see also M. Ajello et al. 2023), bridging the gap between X-ray and gamma-ray observations.

Our results highlight the importance of combining neutrino measurements with photon observations and adopting a multicomponent approach to accurately model the emission from NGC 1068. They also demonstrate that sensitive observations in the MeV regime, along with improved low-energy neutrino detections by future experiments, will be crucial for constraining multimessenger models of this source.

Acknowledgments

The authors would like to thank Chiara Bellenghi and Tomas Kontrimas for helpful discussions relating to the `SkyLLH` software. The authors would like to thank Filippo D'Ammando and David J Thompson for helpful comments as part of the Fermi-LAT collaboration internal review.

The NICER and NuSTAR data shown in this work make use of the data collected by the NICER and NuSTAR missions, and support the NICER GO Cycle 5 proposal run. The Chandra observations are based on archival measurements hosted by the High Energy Astrophysics Science Archive Research Center at doi: 10.25574/cdc.469.

The Fermi-LAT data are provided by NASA Goddard Space Flight Center and supported by the Fermi-LAT Collaboration. The Fermi-LAT Collaboration acknowledges generous ongoing support from a number of agencies and institutes that have supported both the development and the operation of the LAT as well as scientific data analysis. These include the National Aeronautics and Space Administration and the Department of Energy in the United States, the Commissariat à l'Energie Atomique and the Centre National de la Recherche Scientifique/Institut National de Physique Nucléaire et de Physique des Particules in France, the Agenzia Spaziale Italiana and the Istituto Nazionale di Fisica Nucleare in Italy, the Ministry of Education, Culture, Sports, Science and Technology (MEXT), High Energy Accelerator Research Organization (KEK) and Japan Aerospace Exploration Agency (JAXA) in Japan, and the K. A. Wallenberg Foundation, the Swedish Research Council and the Swedish National Space Board in Sweden.

Additional support for science analysis during the operations phase is gratefully acknowledged from the Istituto Nazionale di Astrofisica in Italy and the Centre National

d'Études Spatiales in France. This work was performed in part under DOE Contract DE-AC02-76SF00515.

The IceCube neutrino observations are based on 10 yr of archival data, supported by the Wisconsin IceCube Particle Astrophysics Center and made available by the IceCube Collaboration and hosted by Harvard Dataverse (IceCube Collaboration 2024).

A.D. was supported by an appointment to the NASA Postdoctoral Program at NASA Goddard Space Flight Center, administered by Oak Ridge Associated Universities under contract with NASA. A.D. and J.V. acknowledge support from NICER Guest Observer Cycle 5 (Proposal 6196). J.V. acknowledges support from Vilas Associate funding from the Office of the Vice Chancellor for Research and Graduate Education at the University of Wisconsin–Madison and the National Science Foundation (PHY-2209445 and PHY-2013102). S.M.'s research activities on this project were carried out with contribution of the Next Generation EU funds within the National Recovery and Resilience Plan (PNRR), Mission 4 - Education and Research, Component 2—From Research to Business (M4C2), Investment Line 3.1—Strengthening and creation of Research Infrastructures, Project IR0000012–"CTA+ - Cherenkov Telescope Array Plus". K.F. acknowledges support from the National Science Foundation (PHY-2238916) and the Sloan Research Fellowship. This work was supported by a grant from the Simons Foundation (00001470, KF). J.T. acknowledges support from the National Science Foundation (PHY-2209445). S.H. acknowledges support from the National Science Foundation Graduate Research Fellowship Program (DGE-2039655).

Appendix A
Initial Processing for X-Ray Observations

For each of the X-ray observations used in this work, the initial processing steps required to derive the observations from the data are reported here.

1. *NICER Observations.* The NICER observations are reduced following the standard NICER data reduction technique and data analysis software (NICERDAS v012). The reduction and calibration of the event files were performed using the standard `nicerl2` and `nicerl3-spec` scripts[10] using the response file from CALDB v.20240206. For all NICER observations, no image stacking was performed, as the S/N for all the source observations was sufficiently high. For each NICER observation, the source signal was compared with the background signal estimated using the `3c50` model given by R. A. Remillard et al. (2022).
2. *NuSTAR Observations.* We reduced the NuSTAR observations, which were taken in SCIENCE mode, following the standard NuSTAR data reduction procedure. We used the NuSTAR Data Analysis Software (NUSTARDAS) v2.1.2 to process the data coming from both the NuSTAR cameras, namely Focal Plane Module A (FPMA) and Module B (FPMB). As the observations between the two modules were found to be relatively similar, we used the FPMA data for fitting purposes. We performed the reduction and calibration of the event files using the standard `nupipeline` script, using the response file from the CALDB v.20240104. In each observation, we extracted the source from a circular region centered at the optical position of the source, using a radius $r \sim 150''$, derived via a visual inspection. This ensured that no bright object contaminated the emission from PKS 1502+106. We then extracted the background spectrum from an annular region with an inner radius of $r \sim 180''$ and an outer radius of $r \sim 300''$. We then derived the source and background spectra, as well as the corresponding ancillary response file (ARF) and redistribution matrix file (RMF) by using the `nuproducts` tool.
3. *Chandra Observations.* The Chandra observations are reduced using the `ciao-4.17` tool following the procedure given by the data processing guideline for pointlike sources.[11] A circular region of radius $\sim 3''$ is used to extract the source counts. To derive the background, four circular regions were chosen with a radius of $\sim 5''$–$6''$ with no overlaps with the source or among each other.

Appendix B
Joint X-Ray Spectral Analysis of NGC 1068

A single reflector cannot account for the full 0.5–10 keV X-ray spectrum of NGC 1068, particularly for the coexistence of neutral and He-/H-like iron lines. As shown by M. Guainazzi et al. (1999), S. Bianchi et al. (2001), at least three distinct reflectors are required: a cold, a warm, and a hot one. The cold, optically thick reflector can produce the OVII fluorescent line but requires a low ionization state, insufficient for the higher ionization lines. Conversely, the hot reflector, responsible for the He-/H-like Fe lines, is too ionized to produce lines from lighter elements. Therefore, a third, intermediate-ionization warm reflector is needed to explain features such as Mg, Si, and S lines.

As discussed in the main Section 2, following the approach of I. Pal et al. (2022), we adopt an ionization parameter of $\log \xi = 0$ for the cold (neutral) reflector, and $\log \xi$ is kept free for the warm (ionized) reflector. Our adopted spectral model includes a mekal thermal plasma, a cold reflection component (xillver), an ionized reflection component (xillver with $\log \xi$ kept free), and several emission lines modeled using Gaussian profiles added only when statistically required by the data. In our analysis, the model used in `XSPEC` is expressed as:

$$Model = const * phabs * (mekal + xillver_{cold} + xillver_{warm} + zgauss + zgauss + zgauss + zgauss). \quad \text{(B1)}$$

Here, *const* accounts for the cross-calibration between NICER and Chandra, and phabs models Galactic absorption with $N_{\rm H} = 3.32 \times 10^{20}$ cm^{-2}. All Gaussian lines had free energy and normalization parameters, with line width σ fixed at 0.1 keV. The redshift was held at $z = 0.0038$ (M. P. Véron-Cetty & P. Véron 2010), and the inclination angle fixed at $i = 63°$ (G. Matt et al. 2004). The common parameters between the two reflectors, such as the photon index (Γ), cutoff energy ($E_{\rm cut}$), the iron abundance (AF_e), and the normalization, are tied together. Following G. Matt et al. (2004), we fix $E_{\rm cut}$ to 500 keV.

[10] https://heasarc.gsfc.nasa.gov/docs/nicer/analysis_threads/

[11] https://cxc.cfa.harvard.edu/ciao/threads/pointlike/index.html

Table 4
Best Fit Parameters of the Joint NICER and Chandra Fit for NGC 1068 Discussed in the Appendix

Model	Parameter	Value
mekal	kT_e	$0.75^{+0.09}_{-0.03}$
	abundance	$0.10^{+0.03}_{-0.04}$
	norm ($\times 10^{-2}$)	$1.71^{+0.69}_{-0.30}$
xillver	Γ	$2.12^{+0.17}_{-0.50}$
	$\log \xi$	$1.00^{+0.51}_{-0.31}$
	AF_e	$1.54^{+1.01}_{-0.69}$
	norm ($\times 10^{-4}$)	$3.02^{+0.42}_{-0.25}$
	const	$0.51^{+0.03}_{-0.03}$
	χ^2/dof	201.9/157

Table 5
Best Fit Line Energies along with Normalization Derived for the Joint NICER and Chandra Fit for NGC 1068

Parameter	Line	Value
E1	Fe He-like Kα	$6.74^{+0.08}_{-0.09}$
N_{E1}	⋯	$6.81^{+2.44}_{-2.40}$
E2	Ar XVII	$3.24^{+0.14}_{-0.15}$
N_{E2}	⋯	$1.46^{+0.99}_{-0.95}$
E3	S XV–Si XIV	$2.45^{+0.03}_{-0.03}$
N_{E3}	⋯	$3.97^{+1.61}_{-1.52}$
E4	Si XIII–Si XIV	$1.93^{+0.06}_{-0.05}$
N_{E4}	⋯	$3.76^{+1.74}_{-0.87}$

Note. Here, the line energy (E) is in keV and the normalization (N_E) is in units of 10^{-5} photons keV^{-1} cm^{-2} s^{-1}

The spectral components can be summarized as follows:

1. Cold reflector modeled with xillver (J. García et al. 2014), using $\log \xi = 0$ and $R = -1$ to produce neutral Fe Kα (∼6.4 keV) and Kβ (∼7.06 keV) lines.
2. Warm ionized reflector via xillver with logξ free to vary, representing Compton-scattered reflection from ionized gas.
3. Thermal plasma emission described with mekal, with temperature and abundances free to vary.
4. Emission lines modeled using *zgauss* for Fe XXV (∼6.7 keV), Ar XVII (∼3.2 keV), S XV–Si XIV (∼2.4 keV), and Si XIII–Si XIV (∼1.9 keV).

The best-fit parameters for the continuum are given in Table 4. The emission line parameters are given in Table 5.

Appendix C
SkyLLH Methodology Used in This Work

In this section, we highlight the methodology used to perform the likelihood analysis using `SkyLLH`. This work follows a method similar to the one reported by T. Kontrimas & M. Wolf (2021), C. Bellenghi et al. (2023). If the signal probability density function (PDF) is defined as S_i and the background PDF is defined as B_i, the likelihood function used to derive the probability $p(\boldsymbol{x_i})$ of each observed event $\boldsymbol{x_i}$ is given by

$$\mathcal{L}(n_S, \boldsymbol{x_i}) = \prod_{i=1}^{N} \left[\frac{n_S}{N} S_i(\boldsymbol{x_i}) + \left(1 - \frac{n_S}{N}\right) B_i \right] \quad \text{(C1)}$$

where, n_S is the number of signal events out of a total of N events. The signal PDF $S_i(\boldsymbol{x_i})$ is dependent on the source spectrum chosen. In the event a power-law spectrum is chosen, the signal PDF is dependent on the spectral index γ and x_i and if an LP-like spectrum is chosen, the signal PDF depends on E_{peak} and x_i.

The signal test statistic is then derived using $\text{TS} = -2(\log(\mathcal{L}(n_s = 0) - \log(\mathcal{L}(n_s, \boldsymbol{x_i}))$. As the null hypothesis has no signal events, it is consistent with the background distribution, and a low TS value will signify that no significant events are found, and upper limits are to be reported.

To derive the significance of the fit along with a p-value (denoted as p_{local} in this work), first, a background TS distribution is created by scrambling the data and deriving a TS for each case. The abovementioned signal TS is then used with this background TS distribution to determine the probability (or p-value) of obtaining a TS which matches the signal TS.[12] This p-value is then used to understand the significance of the detection.

ORCID iDs

Abhishek Desai https://orcid.org/0000-0001-7405-9994
Stefano Marchesi https://orcid.org/0000-0001-5544-0749
Justin Vandenbroucke https://orcid.org/0000-0002-9867-6548
Indrani Pal https://orcid.org/0000-0002-7825-1526
Ke Fang https://orcid.org/0000-0002-5387-8138
Dieter Hartmann https://orcid.org/0000-0002-8028-0991
Regina Caputo https://orcid.org/0000-0002-9280-836X
Marco Ajello https://orcid.org/0000-0002-6584-1703
Jessie Thwaites https://orcid.org/0000-0001-9179-3760
Kavic R Kumar https://orcid.org/0000-0002-2068-6949
Sam Hori https://orcid.org/0009-0007-2644-5955

References

Abdo, A. A., Ackermann, M., Ajello, M., et al. 2010, ApJ, 710, 810
Abdollahi, S., Acero, F., Baldini, L., et al. 2022, ApJS, 260, 53
Ajello, M., Murase, K., & McDaniel, A. 2023, ApJL, 954, L49
Bauer, F. E., Arévalo, P., Walton, D. J., et al. 2015, ApJ, 812, 116
Bellenghi, C., Karl, M., & Wolf, M. 2023, ICRC (Nagoya), 38, 1061
Bianchi, S., Matt, G., & Iwasawa, K. 2001, MNRAS, 322, 669
Eichmann, B., Oikonomou, F., Salvatore, S., Dettmar, R.-J., & Becker Tjus, J. 2022, ApJ, 939, 43
Fang, K., Rodriguez, E. L., Halzen, F., & Gallagher, J. S. 2023, ApJ, 956, 8
Fiorillo, D. F. G., Comisso, L., Peretti, E., Petropoulou, M., & Sironi, L. 2024, ApJ, 974, 75
García, J., Dauser, T., Lohfink, A., et al. 2014, ApJ, 782, 76
Gendreau, K. C., Arzoumanian, Z., & Okajima, T. 2012, Proc. SPIE, 8443, 844313
Guainazzi, M., Matt, G., Antonelli, L. A., et al. 1999, MNRAS, 310, 10
HI4PI Collaboration, Ben Bekhti, N., Flöer, L., et al. 2016, A&A, 594, A116
IceCube Collaboration 2024, All-sky Point-source IceCube Data: Years 2008-2018, Harvard Dataverse,
IceCube Collaboration, Aartsen, M., Ackermann, M., et al. 2018, Sci, 361, 147
IceCube Collaboration, Aartsen, M., Ackermann, M., et al. 2020, PhRvL, 124, 051103
IceCube Collaboration, Aartsen, M., Ackermann, M., et al. 2021a, J. Phys. G, 48, 72
IceCube Collaboration, Abbasi, R., Ackermann, M., et al. 2021b, All-sky point-source IceCube data: years 2008-2018 v1, Harvard Dataverse,
IceCube Collaboration, Abbasi, R., Ackermann, M., et al. 2021c, arXiv:2101.09836
IceCube Collaboration, Abbasi, R., Ackermann, M., et al. 2025, ApJ, 988, 141
IceCube Collaboration, Abbasi, R., Ackermann, M., et al. 2025, ApJ, 981, 131
IceCube Collaboration, Fermi-LAT, M.A.G.I.C., et al. 2018, Sci, 361, eaat1378

[12] see also https://user-web.icecube.wisc.edu/~icecube-bootcamp/bootcamp2019/intro_to_stats/Hyp_testing.html.

IceCube Collaboration, Abbasi, R., Ackermann, M., et al. 2022, Sci, 378, 538
Inoue, Y., Khangulyan, D., & Doi, A. 2020, ApJL, 891, L33
Iwasawa, K., Fabian, A. C., & Matt, G. 1997, MNRAS, 289, 443
Khatee Zathul, A., Moulai, M., Fang, K., & Halzen, F. 2025, ApJ, 984, 54
Kontrimas, T., & Wolf, M. 2021, ICRC (Berlin), 37, 1073
Marin, F., et al. 2024, A&A, 689, A238
Matt, G., Bianchi, S., Guainazzi, M., & Molendi, S. 2004, A&A, 414, 155
Matt, G., Guainazzi, M., Frontera, F., et al. 1997, A&A, 325, L13
Murase, K. 2022, ApJL, 941, L17
Murase, K., Kimura, S. S., & Mészáros, P. 2020, PhRvL, 125, 011101
Murase, K., & Stecker, F. W. 2023, The Encyclopedia of Cosmology, Vol. 2 (Singapore: World Scientific), 483
Oikonomou, F., Petropoulou, M., Murase, K., et al. 2021, JCAP, 10, 082
Pal, I., Stalin, C. S., Parker, M. L., Agrawal, V. K., & Marchesi, S. 2022, MNRAS, 517, 3341
Remillard, R. A., Loewenstein, M., Steiner, J. F., et al. 2022, AJ, 163, 130
Rodrigues, X., Garrappa, S., Gao, S., et al. 2021, ApJ, 912, 54
Rodrigues, X., Paliya, V. S., Garrappa, S., et al. 2024, A&A, 681, A119
Romeo, A. B., & Fathi, K. 2016, MNRAS, 460, 2360
Taboada, I., & Stein, R. 2019, ATel, 12967, 1
Véron-Cetty, M. P., & Véron, P. 2010, A&A, 518, A10
Wilks, S. S. 1938, Annals Math. Statist., 9, 60
Willingale, R., Starling, R. L. C., Beardmore, A. P., Tanvir, N. R., & O'Brien, P. T. 2013, MNRAS, 431, 394
Wilson, A. S., Elvis, M., Lawrence, A., & Bland-Hawthorn, J. 1992, ApJL, 391, L75
Yuan, C., Fiorillo, D. F. G., Petropoulou, M., & Liu, Q. 2025, arXiv:2508.08233
Zaino, A., Bianchi, S., Marinucci, A., et al. 2020, MNRAS, 492, 3872
Zhang, H., Fang, K., Li, H., et al. 2019, ApJ, 876, 109